

1                   **Forecasting Tropical Annual Maximum Wet-Bulb  
2                   Temperatures Months in Advance from the Current  
3                   State of El Niño**

4                   **Yi Zhang<sup>1,2</sup>, William R. Boos<sup>1,3</sup>, Isaac Held<sup>4</sup>, Christopher J. Paciorek<sup>5</sup>,  
5                   Stephan Fueglistaler<sup>4,6</sup>**

6                   <sup>1</sup>Department of Earth and Planetary Science, University of California, Berkeley, CA 94720

7                   <sup>2</sup>Miller Institute for Basic Research in Science, University of California, Berkeley, CA 94720

8                   <sup>3</sup>Climate and Ecosystem Sciences Division, Lawrence Berkeley National Laboratory, CA 94720

9                   <sup>4</sup>Program in Atmospheric and Oceanic Sciences, Princeton University, Princeton, NJ 08540

10                  <sup>5</sup>Department of Statistics, University of California, Berkeley, CA 94720

11                  <sup>6</sup>Department of Geosciences, Princeton University, Princeton, NJ 08540

12                  **Key Points:**

- 13                  • Tropical wet-bulb temperatures ( $TW_{max}$ ) peak around five months after El Niño  
14                  winters.
- 15                  • A multiple linear regression model considering the ENSO index and the long-term  
16                  warming trend effectively explains  $TW_{max}$  variability.
- 17                  • Our model quantifies the likelihood of strong El Niño and human-induced warm-  
18                  ing pushing  $TW_{max}$  to record-breaking levels.

19 **Abstract**

20 Humid heatwaves, characterized by high temperature and humidity combinations,  
 21 challenge tropical societies. Extreme wet-bulb temperatures (TW) over tropical land are  
 22 coupled to the warmest sea surface temperatures (SST) by atmospheric convection and  
 23 wave dynamics. Here, we harness this coupling for seasonal forecasts of the annual max-  
 24 imum of daily maximum TW ( $TW_{max}$ ). We develop a multiple linear regression model  
 25 that explains 80% of variance in tropical mean  $TW_{max}$  and significant regional  $TW_{max}$   
 26 variances. The model considers warming trends and El Niño and Southern Oscillation  
 27 (ENSO) indices. Looking ahead, a moderate-to-strong El Niño with an Oceanic Niño In-  
 28 dex (ONI) of 1.5 by the end of 2023 suggests a 42% (11%, 78%) probability of break-  
 29 ing the tropical mean  $TW_{max}$  record in 2024. For an El Niño similar to 2015/2016 (ONI  
 30 of 2.64), the probability escalates to 90% (50%, 99.5%). This approach also holds promise  
 31 for regional  $TW_{max}$  predictions.

32 **Plain Language Summary**

33 The heat and humidity in the tropics can be particularly challenging for people to  
 34 stay comfortable and healthy. This combination of heat and moisture is described us-  
 35 ing a measure called the wet-bulb temperature (TW). We found that these extremely  
 36 humid and hot conditions on land can be predicted about five months in advance using  
 37 a physics-based statistical model. The forecast is possible because the peak of El Niño  
 38 comes before the peak in the warmest sea surface temperatures, which affects the max-  
 39 imum TW on land. This prediction can help tropical societies to better prepare for ex-  
 40 treme heat.

41 **1 Introduction**

42 The tropics, characterized by high temperatures and humidities, face heightened  
 43 risks from heat-related impacts (Sherwood & Huber, 2010; Raymond et al., 2020, 2021;  
 44 Parkes et al., 2022). This vulnerability is exacerbated by the consistent warming trend,  
 45 leading to more frequent and intense heat events. Superimposed on the warming trend  
 46 is the El Niño-Southern Oscillation (ENSO). El Niño events, typified by warmer central  
 47 and eastern equatorial Pacific Ocean temperatures, trigger shifts in atmospheric circu-  
 48 lation that modify global temperature and precipitation patterns (Yulaeva & Wallace,

49 1994). These events often result in more frequent and intense heatwaves in many regions,  
50 including the tropics (Thirumalai et al., 2017; Arblaster & Alexander, 2012; Revadekar  
51 et al., 2009). In contrast, La Niña events, marked by cooler Pacific Ocean temperatures,  
52 tend to bring cooler and wetter conditions. In light of ongoing global warming, an El Niño  
53 event superimposed on the current warming could result in unparalleled hot weather,  
54 underscoring the need for further investigation and preparedness.

55 The physical mechanism underlying pan-tropical land warming during El Niño years  
56 is the free-tropospheric heating that arises from deep convection over anomalously warm  
57 SSTs. This heating causes atmospheric columns over remote land to adjust to a warmer  
58 state in response to the elevated free troposphere temperatures (Brown & Bretherton,  
59 1997; Chiang & Sobel, 2002). Notably, this free-tropospheric warming occurs a few months  
60 after peak El Niños (Pan & Oort, 1983; Sobel et al., 2002; Chiang & Sobel, 2002), as the  
61 SSTs in convective regions (the warmer portions of tropical SSTs) take a few months to  
62 warm following peak El Niño events (Klein et al., 1999; Xie et al., 2009; Fueglistaler, 2019;  
63 Hogikyan et al., 2022).

64 As recognition of humid heat's importance grows, the effects of global warming and  
65 ENSO on extreme humid heat, in addition to extreme temperatures, are emerging as ac-  
66 tive areas of research. Anthropogenic warming is a primary driver of tropical increases  
67 in wet-bulb temperature (TW), a common measure of humid heat (Sherwood & Huber,  
68 2010; Buzan & Huber, 2020; Zhang et al., 2021). According to Zhang et al. (2021), ex-  
69 treme TW in the tropics is projected to rise by 1°C for every 1°C increase in tropical  
70 mean warming due to the mechanism described above. Concurrently, ENSO variability  
71 can significantly impact TW patterns over shorter timeframes (Rogers et al., 2021; Speizer  
72 et al., 2022; Ivanovich et al., 2022). Research has highlighted anomalously high tropi-  
73 cal land mean TW associated with the 1997-1998 El Niño (Raymond et al., 2020; Zhang  
74 et al., 2021), as well as the more frequent occurrence of regional extreme TW during El  
75 Niño years (Rogers et al., 2021; Speizer et al., 2022).

76 In this study, we draw upon existing knowledge that 1) maximum wet-bulb tem-  
77 peratures ( $TW_{max}$ ) over land are influenced by the warmest sea surface temperatures  
78 (SSTs) in the tropics, and 2) a lag of about four months occurs in the warming of the  
79 warmest SSTs after a peak El Niño event. We aim to construct a predictive model for  
80 extreme TW that can provide early warning of extreme  $TW_{max}$  levels several months

in advance. While earlier research has studied the delayed effects of El Niño the following summer in Asia, known as the “Indian Ocean capacitor effect” (Xie et al., 2009), our focus extends to extreme TW in all tropical land areas. Our research aims to enhance seasonal predictions of extreme TW in the tropics, offering more accurate climate risk assessments and enhancing preparedness efforts in these regions.

## 2 Data and Methods

### 2.1 Wet-bulb temperature

Wet-bulb temperatures (TW) are calculated using the ERA5 hourly reanalysis product (Hersbach et al., 2020) by solving the following equation:

$$c_p T_s + L_v q_s = c_p \text{TW} + L_v q_{\text{sat}}(\text{TW}), \quad (1)$$

where  $T_s$  and  $q_s$  represent the 2-meter temperature and 2-meter specific humidity, respectively.  $L_v$  denotes the latent heat of vaporization, and  $c_p$  represents the specific heat capacity of air at constant pressure. In our computations, we use  $c_p$  as 1004.7090 J/kg/K and  $L_v$  as  $2.5008 \times 10^3$  J/kg. Although neglecting the temperature dependence of  $c_p$  and  $L_v$  introduces a small error in TW, it is sufficient for our purposes.

Since the ERA5 dataset does not directly provide the 2-meter specific humidity, we calculate it using the hourly 2-meter dewpoint temperature ( $T_d$ ) and surface pressure ( $p_s$ ), considering the molecular mass ratio of water vapor and air ( $\epsilon$ ) of 0.621981. The specific humidity ( $q_s$ ) is determined as follows:

$$q_s = \frac{\epsilon e_{\text{sat}}(T_d)}{p_s - (1 - \epsilon)e_{\text{sat}}(T_d)}, \quad (2)$$

where  $e_{\text{sat}}$  represents the saturation vapor pressure calculated using the Clausius-Clapeyron equation, specifically the Teten’s formula, consistent with the methodology of the European Centre for Medium-Range Weather Forecasts (ECMWF) (ECMWF, 2014):

$$e_{\text{sat}} = a_1 e^{a_2 \frac{T - T_0}{T - a_3}}, \quad (3)$$

with the parameter values for saturation over water:  $a_1=611.21$  Pa,  $a_2=17.502$ ,  $a_3=32.19$  K, and  $T_0=273.15$  K.

To focus on extreme TW values, we consider the daily maximum TW and then determine the annual maximum, denoting it as  $\text{TW}_{\max}$ .

97        **2.2 ENSO index**

98        The strength of the El Niño-Southern Oscillation (ENSO) phenomenon is assessed  
 99        using the Oceanic Niño Index (ONI), which serves as NOAA's primary index for mon-  
 100        itoring the oceanic component of ENSO. The ONI is calculated as the rolling 3-month  
 101        average temperature anomaly, from the long-term average, of the surface of the east-central  
 102        tropical Pacific near the International Dateline.

103        **3 Results**104        **3.1 ONI leads  $TW_{max}$  by months**

105        To demonstrate that extreme TW over land is controlled by the warmest SSTs through  
 106        the mediation of deep atmospheric convection and free-tropospheric wave dynamics, we  
 107        show the time series of these variables in Figure 1a. All time series are presented as run-  
 108        ning means of 6 months with the monthly climatology removed. The tropical land-average  
 109        of monthly maximum TW exhibits a notable long-term warming trend of approximately  
 110        0.2 K per decade from 1979 to 2022, accompanied by significant interannual variability.  
 111        The monthly average 500-hPa temperature ( $\overline{T_{500}}$ ) and the top 25% of monthly mean SST  
 112        ( $SST_{25\%}$ ) show similar interannual variabilities and long term trends as TW, with con-  
 113        temporaneous peaks. These findings support the notion put forward by Zhang et al. (2021)  
 114        that the warmest SSTs control the maximum TW over land, with the coupling occur-  
 115        ring rapidly enough to render the maximum TW and  $SST_{25\%}$  variations appear nearly  
 116        simultaneous in monthly data.

117        To predict extreme TW over land, we turn our attention to the predictors for the  
 118        warmest 25% of SSTs. ENSO induces significant shifts in atmosphere-ocean circulations,  
 119        altering the energy budget of the ocean's mixed layer and influencing the relatively warm  
 120        SSTs that lie in regions of deep atmospheric convection. The interannual variability in  
 121         $SST_{25\%}$  closely resembles that in the Oceanic Niño Index (ONI), which does not exhibit  
 122        a long-term trend by design. Moreover, major El Niño events coincide with pronounced  
 123        spikes in  $SST_{25\%}$  and  $TW_{max}$  anomalies, with the latter two typically occurring with a  
 124        lag of approximately four months. Notably, the warming of  $TW_{max}$  during the devel-  
 125        oping phase of the 1991-1992 El Niño was interrupted by the aerosol cooling effect of the  
 126        Mt. Pinatubo eruption in June 1991, leading to a missed peak in  $TW_{max}$  despite rising  
 127        ONI. Another significant volcanic eruption, El Chichón in 1982, also coincided with an

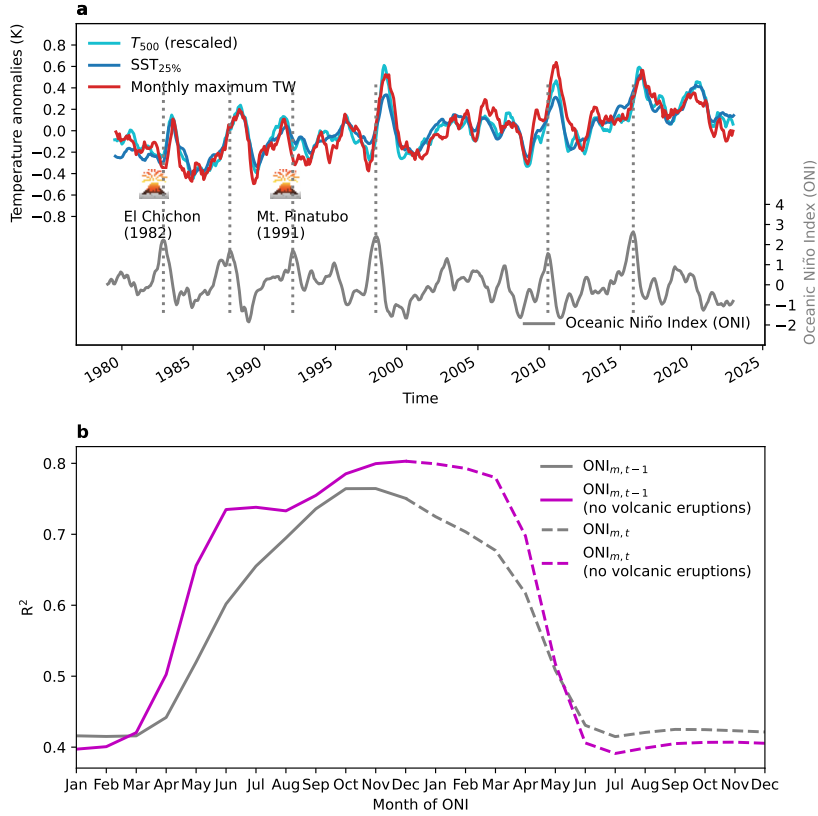


**Figure 1.** ENSO variability leads tropical land  $TW_{max}$  by a few months. **a**, Monthly anomalies of tropical (between  $30^{\circ}\text{S}$  and  $30^{\circ}\text{N}$ ) land mean  $TW_{max}$  (red), the upper-quartile-mean SST (blue) from Hadley Centre Sea Ice and Sea Surface Temperature data set (HadISST) (Rayner et al., 2003), and the average 500-hPa temperature divided by the moist adiabatic amplification factor 1.4 (cyan), as well as the Oceanic Niño Index (ONI) in grey. Timing of strong El Niños ( $ONI > 1.5$ ) are marked with vertical dotted lines. **b**,  $R^2$  values of the multiple linear regression model specified in Eq. (4) using ONI from January to December of preceding years (solid) and contemporaneous years (dashed). The grey line shows the fit using all 43 years between 1990 and 2022, while the magenta line shows the fit of 39 years to exclude major volcanic eruptions.

128 El Niño event. Although elevated  $\text{TW}_{\max}$  values still occurred, they were partially off-  
 129 set by volcanic cooling, and the peak  $\text{TW}_{\max}$  lagged the ONI peak by 9 months. Exclud-  
 130 ing the volcanic eruptions, other major El Niño events consistently precede anomalous  
 131 high  $\text{SST}_{25\%}$  values and, consequently, extreme  $\text{TW}_{\max}$  values. These findings suggest  
 132 the potential to use the ONI to statistically predict  $\text{TW}_{\max}$  some months later, perhaps  
 133 even in the following year.

134 **3.2 Multiple linear regression model of  $\text{TW}_{\max}$**

We develop a multiple linear regression model to predict the annual maximum of daily maximum wet-bulb temperature ( $\text{TW}_{\max}$ ) using two independent variables: a year variable to account for the warming trend and the Oceanic Niño index (ONI) to represent ENSO. The objective is to explain anomalies in  $\text{TW}_{\max}$  as a linear combination of a constantly rising baseline and the ONI from a specific month of the preceding year:

$$\text{TW}_{\max,t} = \beta_0 + \beta_1 t + \beta_2 \text{ONI}_{m,t-1} + \epsilon_t \quad (4)$$

135 Initially, we examine whether this model can capture the tropical land average values  
 136 of  $\text{TW}_{\max}$  between  $30^{\circ}\text{S}$  and  $30^{\circ}\text{N}$ . Even though the exogenous variable is an annual max-  
 137 imum, the process of spatial averaging yields an error term with a near-Gaussian dis-  
 138 tribution, justifying the use of multiple linear regression analysis. We compute the  $R^2$   
 139 values for different months ( $m$ ) in the model using the tropical land average of  $\text{TW}_{\max}$   
 140 from 1980 to 2022, with the year  $t$  and ONI from 1979 to 2021 as the independent vari-  
 141 ables (Figure 1b). The highest  $R^2$  value of 0.764 is obtained when using the ONI from  
 142 all Novembers to predict the land-mean  $\text{TW}_{\max}$  in the following years. However, con-  
 143 sidering the impact of major volcanic eruptions on  $\text{TW}_{\max}$ , we exclude the years affected  
 144 by these eruptions to enhance the accuracy of the linear regression model. We exclude  
 145  $\text{TW}_{\max}$  for the two years following the Mt. Pinatubo eruption (1992 and 1993) and the  
 146 two years following the El Chichón eruption (1983 and 1984). Consequently, we discard  
 147 ONI values from 1982, 1983, 1991, and 1992. The performance of the regression improves,  
 148 with the highest  $R^2$  value of 0.803 achieved using December ONI from the preceding year.  
 149 Notably, the  $R^2$  values exhibit substantial increases from April to August, reaching a rel-  
 150 atively high value of 0.735 in June. This aligns with the spring predictability barrier and  
 151 suggests that a skillful prediction for  $\text{TW}_{\max}$  in the subsequent year might be obtained  
 152 as early as June of the current year.

153 For completeness we also show the  $R^2$  values using ONI for each month of the same  
 154 year as the  $TW_{max}$  in Figure 1b. The explained variance does not increase when using  
 155 ONI of the same year as the occurrence of  $TW_{max}$ . This is because  $TW_{max}$  over land  
 156 is not constrained by the contemporaneous ONI but rather the warmest SSTs which lag  
 157 ONI by a few months.

158 Given the performance of December ONI (years affected by volcanic eruptions ex-  
 159 cluded), all regression in the rest of the paper are against December ONI with the four  
 160 years affected by volcanism removed between 1980 and 2022, resulting in 39 data points  
 161 and two independent variables. Note that the ONI is a three-month running mean, there-  
 162 fore December ONI values contain information from January of the following years; how-  
 163 ever,  $TW_{max}$  occurs in January primarily for some land regions south of 15°S (Figure  
 164 S3), and we later demonstrate predictive skill of the model 3-7 months in advance for  
 165 some sample regions.

166 Figure 2 illustrates the multiple linear regression model in Eq. (4) when  $m$  is De-  
 167 cember. There is negligible multicollinearity between the two independent variables (Fig-  
 168 ure 2a), year ( $t$ ) and ONI of the preceding December ( $ONI_{Dec,t-1}$ ). Each independent  
 169 variable alone explains slightly less than 40% of variance in the tropical mean  $TW_{max}$ .  
 170 Figure 2d shows the observed versus the model-predicted  $TW_{max}$  with 80% of variance  
 171 explained.

### 172 3.3 Impact of warming trend and ENSO variability on $TW_{max}$

173 To assess the relative contributions of warming and ENSO to explaining the vari-  
 174 ance in  $TW_{max}$ , we estimate the standardized regression coefficients ( $\hat{\beta}^*$ ) by carrying out  
 175 the multiple linear regression on standardized variables, with the standardization follow-  
 176 ing  $\frac{x-\bar{x}}{s_x}$  where  $\bar{x}$  denotes the average and  $s_x$  the standard deviation. The standardized  
 177 regression coefficients provide the change in the dependent variable per one-unit change  
 178 in the independent variable measured in standard deviations. The 95% confidence in-  
 179 tervals of the standardized coefficients for the warming trend and ENSO variability are  
 180  $0.65 \pm 0.15$  and  $0.64 \pm 0.15$ , indicating that both factors contribute similarly to the vari-  
 181 ance of the tropical land mean  $TW_{max}$  (Figure 3a).

182 To examine the spatial distribution of these coefficients, we compute  $\hat{\beta}^*$  by regress-  
 183 ing the standardized zonal land mean  $TW_{max}$  (i.e.,  $TW_{max}$  at each grid point zonally

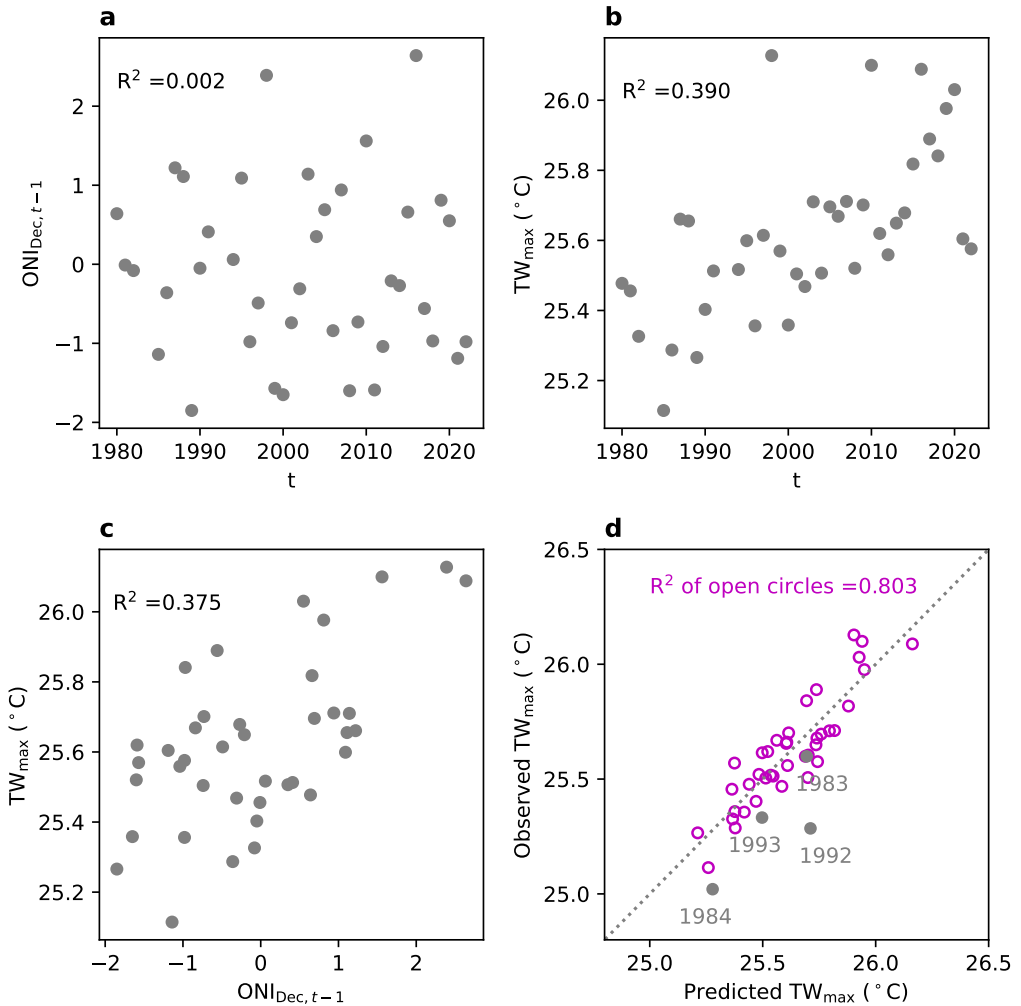


**Figure 2.** Visualization of the multiple linear regression for 30°S-30°N land-mean  $TW_{\max}$ . **a**, Scatter plot of independent variables – December ONI of preceding years ( $ONI_{Dec,t-1}$ ) and year ( $t$ ). **b**, Scatter plot of 30°S-30°N land-mean  $TW_{\max}$  and year ( $t$ ). **c**, Scatter plot of 30°S-30°N land-mean  $TW_{\max}$  and  $ONI_{Dec,t-1}$ . **d**, Actual  $TW_{\max}$  from ERA5 versus the predicted  $TW_{\max}$  by the regression model (open circles). Years following major volcanic eruptions are excluded from the fit and are plotted separately in grey. The grey dotted line indicates 1/1.

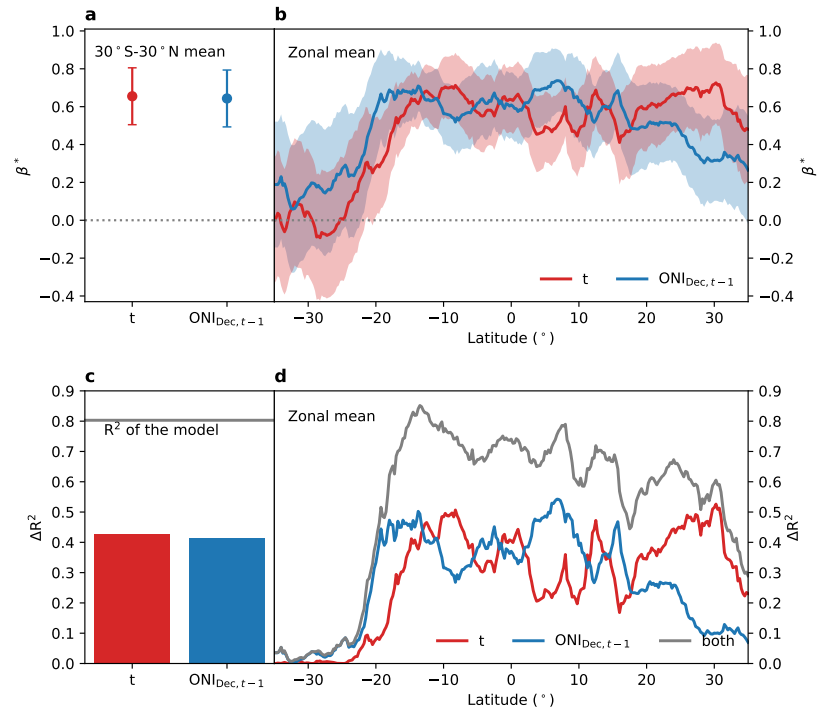


**Figure 3.** Relative importance of constant warming and ENSO variability in explaining  $\text{TW}_{\max}$  variability. **a**, Standardized regression coefficients ( $\hat{\beta}^*$ ) and the 95% confidence intervals for both independent variables. **b**, Same as **a** but for zonal mean  $\text{TW}_{\max}$  over land. **c** and **d**, Incremental  $R^2$  ( $\Delta R^2$ ) for each independent variable, estimated by removing each variable from the full regression, and the  $R^2$  of the full model (grey).

averaged over land only) against the same two standardized independent variables. Figure 3b illustrates the estimated  $\beta^*$  as a function of latitude. Over most latitudes in the tropics, the 95% confidence intervals of  $\hat{\beta}_1^*$  (warming) and  $\hat{\beta}_2^*$  (ENSO) strongly overlap, suggesting a similar contribution at each latitude. However, in the southern subtropics, the magnitude of  $\hat{\beta}^*$  values for both variables declines, and the 95% confidence interval encompasses 0 south of 20°S, indicating that the regression model is not valid in these latitudes. Notably, warming exerts a stronger influence on the northern subtropics compared to ENSO.

The implications of a one-standard-deviation change may differ when the independent variables follow the same type of distribution, as is the case here with the uniformly distributed  $t$  variable and the approximately normally distributed ONI. To provide further evidence and a complementary perspective, we employ an alternative approach by calculating the increment in  $R^2$  ( $\Delta R^2$ ) for each variable:

$$\Delta R_i^2 = R_{\text{full}}^2 - R_{\text{Reduced},i}^2, \quad (5)$$

where  $R_{\text{full}}^2$  represents the  $R^2$  value of the full model (Eq. 4), and  $R_{\text{Reduced},i}^2$  corresponds to the  $R^2$  value when the  $i$ th independent variable is removed from the regression model.  $\Delta R_i^2$  can be loosely regarded as the contribution of the  $i$ th variable to the full model. This method yields similar results (Figure 3c,d), with warming contributing 0.428 and ENSO contributing 0.413 for the tropical mean  $\text{TW}_{\max}$ . The latitudinal patterns of the relative magnitudes of  $\Delta R^2$  values closely resemble those of  $\hat{\beta}^*$ . Furthermore, the  $R^2$  value of the full model indicates that the model performs best in the deep tropics, consistent with empirical findings that support the validity of the weak-temperature-gradient assumption in that latitudinal range (Zhang & Fueglistaler, 2020).

### 3.4 Regional regression

When evaluating the model's performance for gridbox-level annual maxima, the assumption of a Gaussian error term in Eq. (4) becomes less appropriate. In this context, we assume a generalized extreme value (GEV) distribution for the error term and determine the parameters through maximum likelihood estimation (Text S1).

The model's performance exhibits a spatial pattern consistent with the zonal-mean analysis discussed above, with its lowest RMSE values in the deep tropics and an increase towards higher latitudes (Figure 4a).

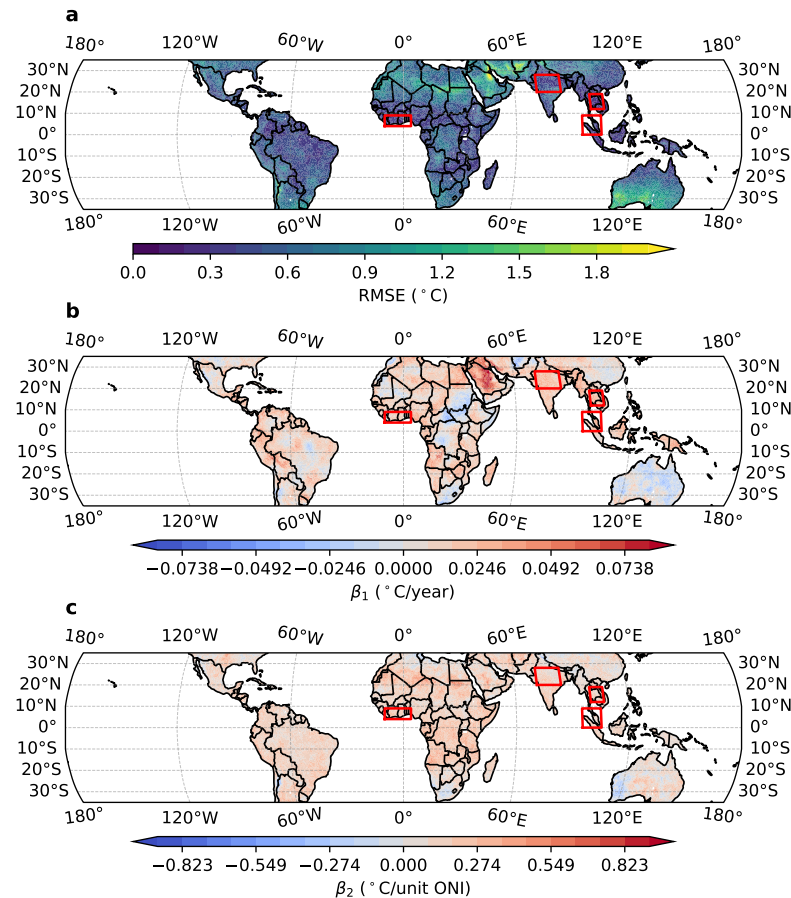


**Figure 4.** Results of fitting the model in Eq 4 at each location. **a**,  $R^2$ . Red boxes outline regions of interest further analyzed in Figure 5. **b**, Standardized regression coefficient of warming. **c**, Standardized regression coefficient of ENSO variability.

The  $\hat{\beta}$  values for both warming (Figure 4b) and ENSO (Figure 4c) are comparable in magnitude when multiplied by the standard deviations of the respective independent variable, implying their similar impacts on  $TW_{max}$  variability across different locations. Contrary to expectations that  $TW_{max}$  in all tropical land is constrained by the warmest SSTs irrespective of place, the coefficient for warming ( $\hat{\beta}_1$ ; Figure 4b) exhibits notable spatial variations. In contrast, the ENSO coefficient ( $\hat{\beta}_2$ ; Figure 4c) is relatively uniform, with El Niños leading to higher  $TW_{max}$  in the following years across most regions. This suggests that, despite El Niño's inherent spatial characteristics, its occurrence induces a relatively uniform response in the following year's continental  $TW_{max}$ .

There are two potential causes of the spatial pattern in the coefficient of warming ( $\hat{\beta}_1$ ): the influence of local land surface conditions, and the uneven response of free-tropospheric temperatures to localized convective heating (Matsuno, 1966; Gill, 1980). Further analysis suggests that the former is more likely, as evidenced by the fact that the areas of negative  $\hat{\beta}_1$  coincide with regions of strongly negative trends in the annual-mean 2-m specific humidity ( $q_s$ ; Figure S1b). Such drying trends could stem from land use change, a process not explored in this study. A drier land surface deepens the planetary boundary layer, distributing surface heat fluxes within a deeper layer and enhancing entrainment of dry free tropospheric air; both of these processes lead to lower boundary layer moist static energy and surface TW (Pal & Eltahir, 2001; Kong & Huber, 2023).

The above analyses illustrate the spatial heterogeneity in the relationships of  $TW_{max}$  with warming and ENSO. While it is reasonably true that tropical  $TW_{max}$  increases over land are uniformly limited by the warmest sea surface temperatures (Zhang et al., 2021), the regional disparities highlight the limitation of this assumption. These results emphasize the importance of conducting localized assessments, which we do next.

We have chosen four regions (marked as red boxes in Figure 4a) to assess how the model in Eq. (4) predicts regional-mean  $TW_{max}$ . The choice of these regions is not governed by any strict rule, but we generally pick regions that exhibit relatively high values in climatological  $TW_{max}$  (Figure S2a) and population density (Figure S2b), and relatively low values in RMSE (Figure 4a). Spatial averaging produces error terms approximating Gaussian distributions, justifying the suitability of applying the multiple linear regression analysis. The model's performance in these smaller regions is depicted in Figure 5b-d, while Figure 5a illustrates the same for the tropical land mean. The model ef-

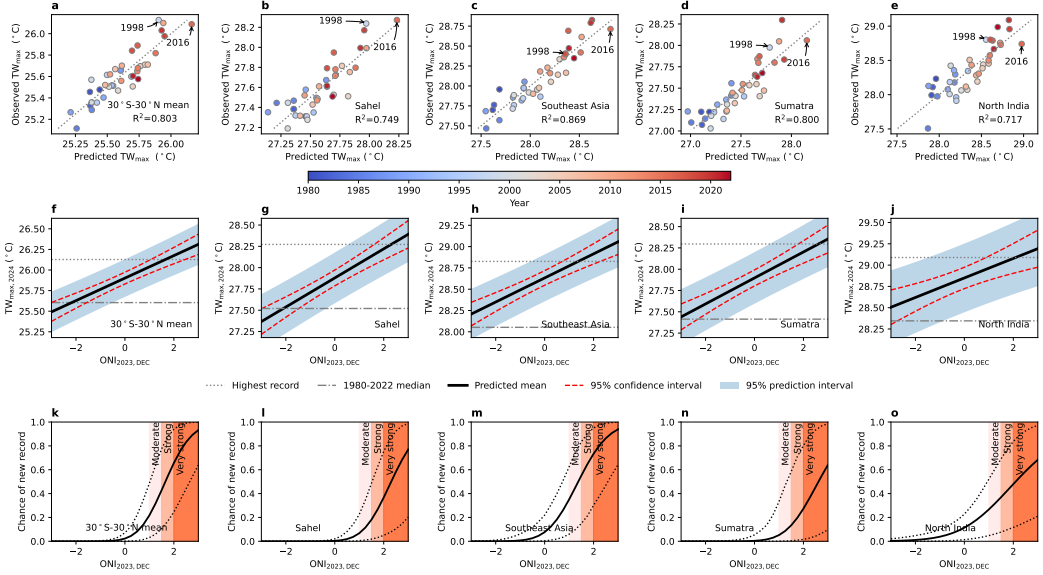


**Figure 5.** Example  $TW_{max}$  forecast for 2024. **a-e**, Performance of multiple linear regression for  $30^{\circ}\text{S}$ - $30^{\circ}\text{N}$  land mean and four regions marked in Figure 4a. Color indicates the year of the data point. Two major El Niños-1998 and 2016-are highlighted. **f-j**, Predicted  $TW_{max,2024}$  as a function of December ONI, 2023. Confidence intervals in red account for the standard error of the predicted mean. Prediction intervals in blue additionally take into account the year-to-year variability around the predicted mean. **k-o**, Estimated chance of  $TW_{max}$  setting new records in 2024 in the tropical mean and each region conditioned upon the strength of El Niño by the end of 2023. ONI ranges of moderate ( $1.0 \leq \text{ONI} < 1.5$ ), strong ( $1.5 \leq \text{ONI} < 2.0$ ) and very strong ( $\text{ONI} \geq 2.0$ ) El Niño events are marked.

**Table 1.** Summary of multiple linear regression results<sup>a</sup>

Region	30°S-30°N mean	Sahel	Southeast Asia	Sumatra	North India
$\hat{\beta}_1$ (°C/year)	0.0125±0.0029 <sup>b</sup>	0.0121±0.0037	0.0235±0.0034	0.0184±0.0038	0.0218±0.0050
$\hat{\beta}_2$ (°C/unit ONI)	0.137±0.032	0.171±0.042	0.141±0.038	0.152±0.042	0.115±0.056
$\hat{\beta}_1^*$ (standardized $\hat{\beta}_1$ )	0.65	0.55	0.84	0.73	0.78
$\hat{\beta}_2^*$ (standardized $\hat{\beta}_2$ )	0.64	0.70	0.45	0.55	0.37
$\Delta R_1^2$	0.428	0.300	0.700	0.538	0.607
$\Delta R_1^2$	0.413	0.483	0.203	0.298	0.135
$R^2$	0.803	0.749	0.869	0.800	0.716
F-statistic, P>F	73.36, 2.0e-13	53.66, 1.6e-11	119.3, 1.3e-16	72.04, 2.6e-13	45.50, 1.4e-10
t, P> t  for $\hat{\beta}_1$	8.844, 1.5e-10	6.557, 1.3e-07	13.859, 5.3e-16	9.843, 9.5e-12	8.783, 1.8e-10
t, P> t  for $\hat{\beta}_2$	8.686, 2.3e-10	8.321, 6.6e-10	7.465, 8.1e-9	7.328, 1.2e-8	4.134, 2.0e-4
Root Mean squared error (RMSE; °C) <sup>c</sup>	0.103	0.134	0.124	0.136	0.182
Leave-one-out cross-validation RMSE (°C)	0.113(+9.45%) <sup>d</sup>	0.147(+9.17%)	0.135(+8.86%)	0.149(+9.05%)	0.199(+9.71%)
Walk-forward validation RMSE (°C)	0.119(+7.08%) <sup>e</sup>	0.138(+20.1%)	0.156(+17.6%)	0.171(+18.8%)	0.194(+17.6%)
Record-setting probability (ONI=1.5)	42%(11%-78%) <sup>f</sup>	15%(1.8%-49%)	56%(15%-84%)	11%(0.5%-58%)	35%(7.7%-69%)
Record-setting probability (ONI=2.64)	90%(50%-99.5%)	66%(14%-95%)	92%(55%-99.5%)	51%(5.5%-95%)	63%(17%-94%)

<sup>a</sup> Number of Observations: 39; Residuals degree of freedom: 36; Model degree of freedom: 3<sup>b</sup> 95% confidence interval<sup>c</sup> Maximum likelihood estimate of MSE, not the unbiased MSE, is used throughout the paper<sup>d</sup> Percentage change compared to the regression model with all 39 data points<sup>e</sup> Percentage change of RMSE of the last 19 data points<sup>f</sup> 95% BCa bootstrap interval

effectively explains  $TW_{max}$  variability at both regional and tropical mean scales. The contributions of warming and ENSO exhibit regional variations, as evidenced by the range of  $\Delta R^2$  values in Table 1. In Southeast Asia, for instance, the variability of  $TW_{max}$  is predominantly influenced by the warming trend, with higher  $TW_{max}$  values occurring in more recent years (Figure 5c). Conversely, the Sahel region exhibits stronger sensitivity to ENSO variability, with 1998 and 2016 having the highest  $TW_{max}$  (Figure 5b).

$TW_{max}$  occur at different times of year in different regions. A general pattern emerges, with  $TW_{max}$  events occurring during boreal summer (June-August) north of 15°N, boreal winter (December-February) south of 15°S, and boreal spring (March-May) and fall (September-November) between 15°S and 15°N (Figure S3a). For the four selected regions,  $TW_{max}$  typically occurs in April for Sahel, May for Southeast Asia and Sumatra, and June to August for North India (Figure S3b). The multiple linear regression model thus demonstrates an average lead time of approximately five months for tropical land areas and a range of three to seven months for the four regions of interest.

255        **3.5 Forecasting  $TW_{max}$  months in advance**

256        Before making predictions with the multiple linear regression model, we assess its  
 257        predictive skill using leave-one-out cross-validation and walk-forward validation which  
 258        is more suitable for time series data. This is motivated by the possibility of overfitting,  
 259        especially since our model was trained using the full dataset. The moderate increases  
 260        in RMSE during cross-validation (Table 1) suggest that the model is not seriously over-  
 261        fitted and is suitable for making predictions with details provided in Text S2 and Fig-  
 262        ures S4.

Our objective is to generate a forecast of  $TW_{max}$  for the upcoming year based on the December Oceanic Niño Index (ONI) of the current year. Note that the ONI is a three-month running mean, with December ONI of the current year technically containing information from January of the upcoming year, but nearly all land north of  $15^{\circ}\text{S}$  has  $TW_{max}$  occurring in March or later of the upcoming year (Figure S3b). Taking the year 2024 as an example, the predicted mean depends on  $\text{ONI}_{\text{Dec},2023}$  following:

$$\hat{TW}_{\text{max},2024} = \hat{\beta}_0 + 2024\hat{\beta}_1 + \hat{\beta}_2\text{ONI}_{\text{Dec},2023}. \quad (6)$$

263        Figure 5e-h presents the 95% confidence intervals of the predicted mean and the  
 264        95% prediction intervals of  $TW_{\text{max},2024}$  as a function of  $\text{ONI}_{\text{Dec},2023}$  (Text S3). As ex-  
 265        pected, even in a neutral ENSO state, the mean predicted  $TW_{\text{max},2024}$  values in all four  
 266        regions (Figure 5f-h) as well as the tropical mean (Figure 5e) surpass the median of past  
 267        records. This demonstrates the influence of the cumulative warming at the present level  
 268        on  $TW_{\text{max}}$ . A rough estimate of the impact of warming since 1980 on  $TW_{\text{max}}$  is the num-  
 269        ber of years (44 years) multiplied by  $\hat{\beta}_1$ , yielding 0.55 K for the tropical mean. The ONI  
 270        value required to achieve a comparable effect can be estimated by dividing the warming-  
 271        induced increase in  $TW_{\text{max}}$  by  $\hat{\beta}_2$ . Remarkably, an ONI value of 4.0, representing a su-  
 272        per El Niño of unprecedented magnitude, would be necessary to match the increase in  
 273        tropical mean  $TW_{\text{max}}$  caused by cumulative warming. Although this estimation is not  
 274        rigorous, it provides an estimate of the magnitude of the cumulative warming effect since  
 275        1980, equivalent to an exceptionally strong El Niño.

276        Next, we estimate the probability of a new  $TW_{\text{max}}$  record being set in 2024, as-  
 277        suming knowledge of  $\text{ONI}_{\text{Dec},2023}$ . Rigorously estimating this probability is challenging,  
 278        and our estimate is contingent upon certain assumptions. We assume that the predicted

279 TW<sub>max</sub> at each  $\mathbf{x}_p = (1, 2024, \text{ONI}_{\text{Dec},2023})^T$  follows a Gaussian distribution centering  
 280 at the predicted mean given by Equation (6) with a standard deviation equalling the root  
 281 mean squared error (RMSE; we use the maximum likelihood estimate of RMSE rather  
 282 than the unbiased estimate). For each ONI<sub>Dec,2023</sub> value, we then compute the area un-  
 283 der this Gaussian distribution when the predicted TW<sub>max</sub> exceeds the highest record,  
 284 resulting in the central estimates of the probability of a new TW<sub>max</sub> record being set (solid  
 285 lines in Figures 5i-l). The 95% confidence intervals for this probability, shown as dot-  
 286 ted lines in Figures 5i-l, were derived using the bias-corrected and accelerated (BCa) boot-  
 287 strap method (Text S4).

288 For the tropical mean TW<sub>max</sub>, an Oceanic Niño Index (ONI) of 1.5 by the end of  
 289 2023 leads to a central estimate of a 42% probability of surpassing the TW<sub>max</sub> record  
 290 in 2024 with the 95% confidence interval ranging from 11% to 78% (Figure 5k). In con-  
 291 trast, if an El Niño as intense as the 2015/2016 event (with an ONI of 2.64) occurs, the  
 292 central probability estimate increases to 90%, with the 95% confidence interval ranging  
 293 from 50% to 99.5% (Figure 5k). These probabilities as well as the width of the confidence  
 294 intervals exhibit regional variability (Table 1), with Southeast Asia emerging as a region  
 295 with an elevated likelihood of experiencing record-breaking TW<sub>max</sub> during a strong El  
 296 Niño (Figure 5m, Table 1).

## 297 4 Summary and Discussion

298 This study establishes the potential for dynamically based predictions of the an-  
 299 nual maximum of daily maximum wet-bulb temperatures (TW<sub>max</sub>) across tropical land  
 300 areas with an average lead time of five months. This predictability arises from two facts  
 301 in tropical atmosphere-ocean dynamics: 1) TW<sub>max</sub> over tropical land is closely coupled  
 302 to free tropospheric temperature through deep convection and tropical wave dynamics,  
 303 and 2) the free tropospheric temperature is determined by the warmest SSTs, which typ-  
 304 ically reach their peak around five months after the peak of an El Niño event (Pan &  
 305 Oort, 1983; Sobel et al., 2002; Chiang & Sobel, 2002).

306 By using the Oceanic Niño Index (ONI) as a predictor and accounting for the warm-  
 307 ing trend through a “year” variable, our multiple linear regression model effectively ex-  
 308 plains a substantial portion—80%—of the variability in tropical land mean TW<sub>max</sub>. Al-  
 309 though the model’s performance varies across regions, it demonstrates promising skills,

especially in the deep tropics (Figures 3b,d, Figure 4a). Both warming trends and ENSO have contributed significantly to the variability in  $TW_{max}$ , and our analysis shows that the cumulative warming effect since 1980 is comparable to that of an exceptionally strong El Niño.

We forecasted  $TW_{max}$  for the year 2024 assuming knowledge of the December ONI of 2023 and estimated the probability of setting new  $TW_{max}$  records in 2024. The strength of an El Niño event significantly influences the probability of breaking  $TW_{max}$  records. The tropical mean and regional variations in these probabilities are detailed in Figure 5k-o and Table 1.

Although TW may not be the most precise metric for evaluating heat stress (Lu & Romps, 2023; Baldwin et al., 2023), the methodology developed in this work has the potential to be adapted to temperature and Heat Index, which are influenced by SST through similar dynamics (Chiang & Sobel, 2002; Byrne, 2021).

Finally, this study calls for increased efforts to enhance the accuracy of predictions of ENSO-induced free-tropospheric temperature variations. Improved predictions for free-tropospheric temperatures, such as  $T_{500}$ , could benefit projections of extreme heat stress across tropical continents, as illustrated by the close correlation between the two in Figure 1a. Note that the predictive model proposed in this study does not rely on forecasting future ENSO events; it leverages only the current ENSO state. This model's predictive skill originates from the time lag between tropical tropospheric temperatures and ENSO variability. That said, advances in ENSO forecasting could further extend the lead times at which accurate  $TW_{max}$  predictions become feasible.

### Acknowledgments

Y.Z. acknowledges the support from the Miller Institute for Basic Research in Science at the University of California, Berkeley. This research was partially supported by the Director, Office of Science, Office of Biological and Environmental Research of the U.S. Department of Energy as part of the Regional and Global Model Analysis program area within the Earth and Environmental Systems Modeling Program under Contract No. DE-AC02-05CH11231 and used resources of the National Energy Research Scientific Computing Center (NERSC), also supported by the Office of Science of the U.S. Department of Energy, under Contract No. DE-AC02-05CH11231. The authors thank the Statisti-

341       cal Consulting provided by the Department of Statistics at the University of California  
 342       Berkeley, represented by Hyunsuk Kim and James B. Brown, and Mark Risser for their  
 343       valuable feedback on the statistical approaches.

344       **Open Research**

345       The Oceanic Niño Index (ONI) is provided by National Oceanic and Atmospheric  
 346       Administration's Climate Prediction Center and is available here: [https://origin.cpc.ncep.noaa.gov/products/analysis\\_monitoring/ensostuff/ONI\\_v5.php](https://origin.cpc.ncep.noaa.gov/products/analysis_monitoring/ensostuff/ONI_v5.php). The ERA5  
 347       hourly data on pressure levels and single levels from 1979 to present are downloaded from  
 348       the Copernicus Climate Change Service Climate Data Store (<https://cds.climate.copernicus.eu>). The Hadley Centre Sea Ice and Sea Surface Temperature data set (HadISST) is  
 349       downloaded from <https://www.metoffice.gov.uk/hadobs/hadisst/>.

352       **References**

- 353       Arblaster, J. M., & Alexander, L. V. (2012). The impact of the el niño-southern  
 354       oscillation on maximum temperature extremes. *Geophysical Research Letters*,  
 355       39(20).
- 356       Baldwin, J. W., Benmarhnia, T., Ebi, K. L., Jay, O., Lutsko, N. J., & Vanos, J. K.  
 357       (2023). Humidity's role in heat-related health outcomes: A heated debate.  
 358       *Environmental Health Perspectives*, 131(5), 055001.
- 359       Brown, R. G., & Bretherton, C. S. (1997). A test of the strict quasi-equilibrium the-  
 360       ory on long time and space scales. *Journal of the atmospheric sciences*, 54(5),  
 361       624–638.
- 362       Buzan, J. R., & Huber, M. (2020). Moist heat stress on a hotter earth. *Annual Re-  
 363       view of Earth and Planetary Sciences*, 48, 623–655.
- 364       Byrne, M. P. (2021). Amplified warming of extreme temperatures over tropical land.  
 365       *Nature Geoscience*, 14(11), 837–841.
- 366       Chiang, J. C., & Sobel, A. H. (2002). Tropical tropospheric temperature variations  
 367       caused by enso and their influence on the remote tropical climate. *Journal of  
 368       climate*, 15(18), 2616–2631.
- 369       ECMWF, S. P. (2014). In ifs documentation cy40r1 part iv: Physical processes.  
 370       *ECMWF: Reading, UK*, 111–113.
- 371       Fueglistaler, S. (2019). Observational evidence for two modes of coupling between

- 372 sea surface temperatures, tropospheric temperature profile, and shortwave  
373 cloud radiative effect in the tropics. *Geophysical Research Letters*, 46(16),  
374 9890–9898.
- 375 Gill, A. E. (1980). Some simple solutions for heat-induced tropical circulation. *Quarterly  
376 Journal of the Royal Meteorological Society*, 106(449), 447–462.
- 377 Hersbach, H., Bell, B., Berrisford, P., Hirahara, S., Horányi, A., Muñoz-Sabater, J.,  
378 ... others (2020). The era5 global reanalysis. *Quarterly Journal of the Royal  
379 Meteorological Society*, 146(730), 1999–2049.
- 380 Hogikyan, A., Resplandy, L., & Fueglistaler, S. (2022). Cause of the intense tropics-  
381 wide tropospheric warming in response to el niño. *Journal of Climate*, 35(10),  
382 2933–2944.
- 383 Ivanovich, C., Anderson, W., Horton, R., Raymond, C., & Sobel, A. (2022). The  
384 influence of intraseasonal oscillations on humid heat in the persian gulf and  
385 south asia. *Journal of Climate*, 35(13), 4309–4329.
- 386 Klein, S. A., Soden, B. J., & Lau, N.-C. (1999). Remote sea surface temperature  
387 variations during enso: Evidence for a tropical atmospheric bridge. *Journal of  
388 climate*, 12(4), 917–932.
- 389 Kong, Q., & Huber, M. (2023). Regimes of soil moisture-wet bulb temperature cou-  
390 pling with relevance to moist heat stress. *Journal of Climate*, 1–45.
- 391 Lu, Y.-C., & Romps, D. M. (2023). Is a wet-bulb temperature of 35° c the correct  
392 threshold for human survivability? *Environmental Research Letters*, 18(9),  
393 094021.
- 394 Matsuno, T. (1966). Quasi-geostrophic motions in the equatorial area. *Journal of  
395 the Meteorological Society of Japan. Ser. II*, 44(1), 25–43.
- 396 Pal, J. S., & Eltahir, E. A. (2001). Pathways relating soil moisture conditions to  
397 future summer rainfall within a model of the land–atmosphere system. *Journal  
398 of Climate*, 14(6), 1227–1242.
- 399 Pan, Y. H., & Oort, A. H. (1983). Global climate variations connected with sea  
400 surface temperature anomalies in the eastern equatorial pacific ocean for the  
401 1958–73 period. *Monthly Weather Review*, 111(6), 1244–1258.
- 402 Parkes, B., Buzan, J. R., & Huber, M. (2022). Heat stress in africa under high in-  
403 tensity climate change. *International journal of biometeorology*, 66(8), 1531–  
404 1545.

- 405 Raymond, C., Matthews, T., & Horton, R. M. (2020). The emergence of heat and  
406 humidity too severe for human tolerance. *Science Advances*, 6(19), eaaw1838.
- 407 Raymond, C., Matthews, T., Horton, R. M., Fischer, E. M., Fueglistaler, S.,  
408 Ivanovich, C., ... Zhang, Y. (2021). On the controlling factors for globally  
409 extreme humid heat. *Geophysical Research Letters*, 48(23), e2021GL096082.
- 410 Rayner, N., Parker, D. E., Horton, E., Folland, C. K., Alexander, L. V., Rowell, D.,  
411 ... Kaplan, A. (2003). Global analyses of sea surface temperature, sea ice,  
412 and night marine air temperature since the late nineteenth century. *Journal of*  
413 *Geophysical Research: Atmospheres*, 108(D14).
- 414 Revadekar, J., Kothawale, D., & Rupa Kumar, K. (2009). Role of el niño/la niña  
415 in temperature extremes over india. *International Journal of Climatology: A*  
416 *Journal of the Royal Meteorological Society*, 29(14), 2121–2129.
- 417 Rogers, C. D., Ting, M., Li, C., Kornhuber, K., Coffel, E. D., Horton, R. M., ...  
418 Singh, D. (2021). Recent increases in exposure to extreme humid-heat events  
419 disproportionately affect populated regions. *Geophysical Research Letters*,  
420 48(19), e2021GL094183.
- 421 Sherwood, S. C., & Huber, M. (2010). An adaptability limit to climate change  
422 due to heat stress. *Proceedings of the National Academy of Sciences*, 107(21),  
423 9552–9555.
- 424 Sobel, A. H., Held, I. M., & Bretherton, C. S. (2002). The enso signal in tropical  
425 tropospheric temperature. *Journal of climate*, 15(18), 2702–2706.
- 426 Speizer, S., Raymond, C., Ivanovich, C., & Horton, R. M. (2022). Concentrated and  
427 intensifying humid heat extremes in the ipcc ar6 regions. *Geophysical Research*  
428 *Letters*, 49(5), e2021GL097261.
- 429 Thirumalai, K., DiNezio, P. N., Okumura, Y., & Deser, C. (2017). Extreme tem-  
430 peratures in southeast asia caused by el niño and worsened by global warming.  
431 *Nature communications*, 8(1), 15531.
- 432 Xie, S.-P., Hu, K., Hafner, J., Tokinaga, H., Du, Y., Huang, G., & Sampe, T. (2009).  
433 Indian ocean capacitor effect on indo–western pacific climate during the sum-  
434 mer following el niño. *Journal of climate*, 22(3), 730–747.
- 435 Yulaeva, E., & Wallace, J. M. (1994). The signature of enso in global temperature  
436 and precipitation fields derived from the microwave sounding unit. *Journal of*  
437 *climate*, 7(11), 1719–1736.

438 Zhang, Y., & Fueglistaler, S. (2020). How tropical convection couples high moist  
439 static energy over land and ocean. *Geophysical Research Letters*, 47(2),  
440 e2019GL086387.

441 Zhang, Y., Held, I., & Fueglistaler, S. (2021). Projections of tropical heat stress con-  
442 strained by atmospheric dynamics. *Nature Geoscience*, 14(3), 133–137.

# Supporting Information for “Forecasting Tropical Annual Maximum Wet-Bulb Temperatures Months in Advance from the Current State of El Niño”

Yi Zhang<sup>1,2</sup>, William R. Boos<sup>1,3</sup>, Isaac Held<sup>4</sup>, Christopher J. Paciorek<sup>5</sup>,

Stephan Fueglistaler<sup>4,6</sup>

<sup>1</sup>Department of Earth and Planetary Science, University of California, Berkeley, CA 94720

<sup>2</sup>Miller Institute for Basic Research in Science, University of California, Berkeley, CA 94720

<sup>3</sup>Climate and Ecosystem Sciences Division, Lawrence Berkeley National Laboratory, CA 94720

<sup>4</sup>Program in Atmospheric and Oceanic Sciences, Princeton University, Princeton, NJ 08540

<sup>5</sup>Department of Statistics, University of California, Berkeley, CA 94720

<sup>6</sup>Department of Geosciences, Princeton University, Princeton, NJ 08540

## Contents of this file

1. Text S1 to S4
2. Figures S1 to S4

## Text S1. Fitting generalized extreme value distributions

---

The generalized extreme value (GEV) distribution is represented by the probability density function:

$$f(x; \mu, \sigma, \xi) = \begin{cases} \exp\left(-\left[1 + \xi\left(\frac{x-\mu}{\sigma}\right)\right]^{-1/\xi}\right) \left[1 + \xi\left(\frac{x-\mu}{\sigma}\right)\right]^{-(\frac{1}{\xi}+1)} \frac{1}{\sigma}, & \text{for } \xi \neq 0, \\ \exp\left(-\exp\left(\frac{-(x-\mu)}{\sigma}\right)\right) \exp\left(\frac{-(x-\mu)}{\sigma}\right) \frac{1}{\sigma}, & \text{for } \xi = 0. \end{cases} \quad (1)$$

In our model, the location parameter,  $\mu$ , is defined as a linear combination of the year ( $t$ ) and the Oceanic Niño Index from the preceding December ( $\text{ONI}_{t-1}$ ):

$$\mu = \beta_0 + \beta_1 t + \beta_2 \text{ONI}_{t-1} \quad (2)$$

Thus, the log-likelihood function, given the data, can be expressed as:

$$L(\beta_0, \beta_1, \beta_2, \sigma, \xi | \text{TW}_{\max,1}, \dots, \text{TW}_{\max,n}, t_1, \dots, t_n, \text{ONI}_0, \dots, \text{ONI}_{t-1})$$

$$= \begin{cases} -n \ln \sigma - (1 + \frac{1}{\xi}) \sum_{t=1}^n \ln(1 + \xi \frac{\text{TW}_{\max} - \beta_0 - \beta_1 t - \beta_2 \text{ONI}_{t-1}}{\sigma}) - \sum_{t=1}^n (1 + \xi \frac{\text{TW}_{\max} - \beta_0 - \beta_1 t - \beta_2 \text{ONI}_{t-1}}{\sigma})^{-\frac{1}{\xi}} & \text{if } \xi \neq 0 \\ -n \ln \sigma - \sum_{t=1}^n \frac{\text{TW}_{\max} - \beta_0 - \beta_1 t - \beta_2 \text{ONI}_{t-1}}{\sigma} - \sum_{t=1}^n \exp(-\frac{\text{TW}_{\max} - \beta_0 - \beta_1 t - \beta_2 \text{ONI}_{t-1}}{\sigma}) & \text{if } \xi = 0 \end{cases}$$

To obtain optimal parameter values, the negative log-likelihood ( $-L$ ) is minimized using the “minimize” function from Python’s “scipy” package. The estimated  $\hat{\beta}$  values derived this way, as well as the Mean Squared Error (MSE), are quite similar to those from a standard multiple linear regression (not shown).

## Text S2. Cross-validation of the regression model

Before generating predictions with the multiple linear regression model, we evaluate its predictive performance through leave-one-out cross-validation and walk-forward validation.

The leave-one-out cross-validation results in a 9.4% increase in the Root Mean Squared Error (RMSE) for the tropical mean. Similarly, the increase in RMSE ranges from 8.9% to 9.7% for each of the four focus regions, as shown in Table 1.

For the walk-forward validation, we use the first 20 data points as the training set and progressively add one data point to the training set. The validation set comprises the one data point immediately following the training set. The results are presented in Figure S4 and Table 1. The RMSE for the last 19 data points shows a 7.1% increase for the tropical mean and ranges from 17.6% to 20.1% for the four regions.

These moderate increases in RMSE from both the leave-one-out cross-validation and walk-forward validation suggest that the model is not seriously overfitted.

### **Text S3. Confidence intervals and prediction intervals**

The 95% confidence interval of the predicted mean  $\hat{TW}_{max}$  is calculated as:

$$\hat{TW}_{max} \pm t_{0.025,36} \text{ se}(\hat{TW}_{max}) \quad (3)$$

where the  $t$  value of a two-sided significance level of 0.05 with 36 degrees of freedom is 2.028. The 95% prediction interval is given by:

$$\hat{TW}_{max} \pm t_{0.025,36} \sqrt{\text{MSE} + \text{se}(\hat{TW}_{max})^2}, \quad (4)$$

where the standard error of fit at  $\mathbf{x}_p = (1, 2024, \text{ONI}_{\text{Dec},2023})^T$  is determined by

$$\text{se}(\hat{TW}_{max}) = \sqrt{\text{MSE}(\mathbf{x}_p^T (X^T X)^{-1} \mathbf{x}_p)} \quad (5)$$

with MSE being the mean squared error and  $X$  being the  $39 \times 3$  regressor matrix:

$$X = \begin{bmatrix} 1 & 1980 & \text{ONI}_{\text{Dec},1979} \\ 1 & 1981 & \text{ONI}_{\text{Dec},1980} \\ 1 & 1982 & \text{ONI}_{\text{Dec},1981} \\ 1 & 1985 & \text{ONI}_{\text{Dec},1984} \\ \vdots & \vdots & \vdots \\ 1 & 1991 & \text{ONI}_{\text{Dec},1990} \\ 1 & 1994 & \text{ONI}_{\text{Dec},1993} \\ \vdots & \vdots & \vdots \\ 1 & 2022 & \text{ONI}_{\text{Dec},2021} \end{bmatrix}. \quad (6)$$

#### Text S4. Confidence intervals for the exceedance probability

We calculate the confidence intervals of the probability by bootstrapping the original 39 data points and associated covariate values (a nonparametric bootstrap). For each of the 9999 bootstrap replicates, we estimate the probability of exceeding the previous record using the multiple linear regression model. Specifically, we assume that the predicted  $\text{TW}_{\max}$  at each  $\mathbf{x}_p = (1, 2024, \text{ONI}_{\text{Dec},2023})^T$  follows a Gaussian distribution centering at the predicted mean given by Equation (6) with a standard deviation equalling the root mean squared error (RMSE). For each  $\text{ONI}_{\text{Dec},2023}$  value, we then compute the area under this Gaussian distribution when the predicted  $\text{TW}_{\max}$  exceeds the highest record, resulting in the probability of a new  $\text{TW}_{\max}$  record being set for this replicate. Given the potential skewness of the probability distribution when the central estimate approaches 0 or 1, we employ the bias-corrected and accelerated (BCa) method for bootstrap confidence intervals. The BCa bootstrap analysis is conducted using the R “boot” package.

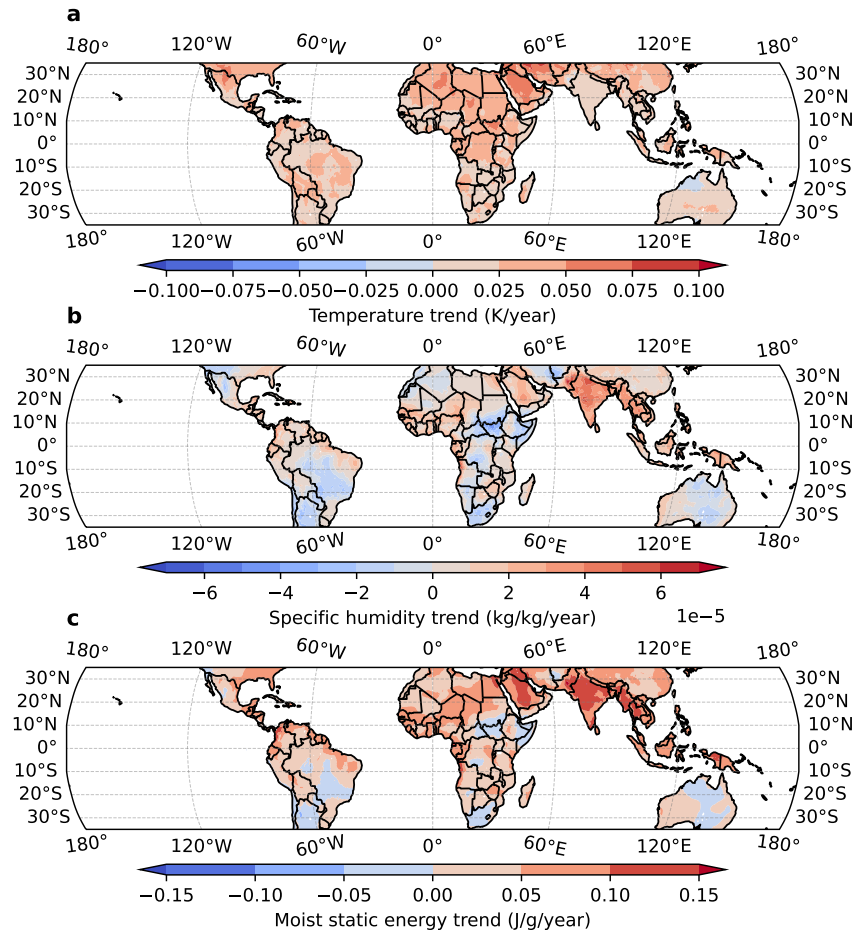


**Figure S1.** Linear trends of annual-mean 2-m air temperature (**a**), specific humidity (**b**), and moist static energy (**c**) from 1979 to 2022 according to ERA5.

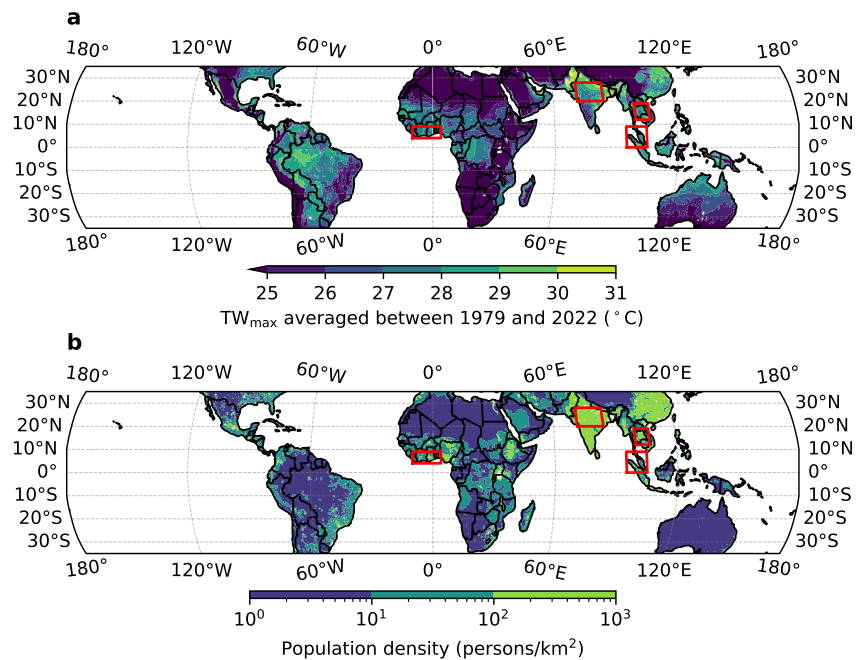


**Figure S2.** **a**, Climatology of the annual maximum TW (TW<sub>max</sub>) between 1979 and 2022.

The color scale only distinguishes values greater than 25°C. **b**, Population density map acquired from [https://neo.gsfc.nasa.gov/view.php?datasetId=SEDAC\\_POP](https://neo.gsfc.nasa.gov/view.php?datasetId=SEDAC_POP).

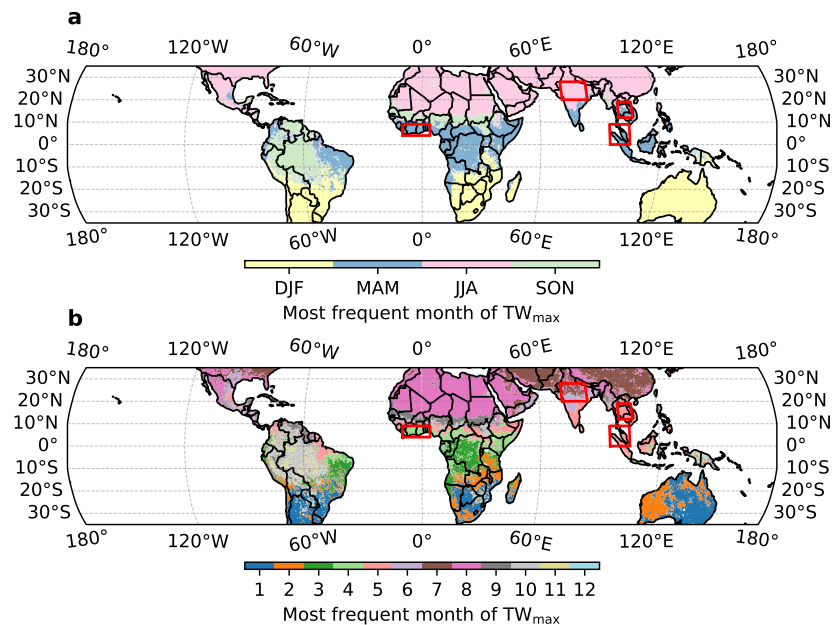


**Figure S3.** The most common month for the occurrence of annual maximum TW for each location. Groupings of three months (DJF, MAM, JJA, SON) are shown in **b**, along with individual months.

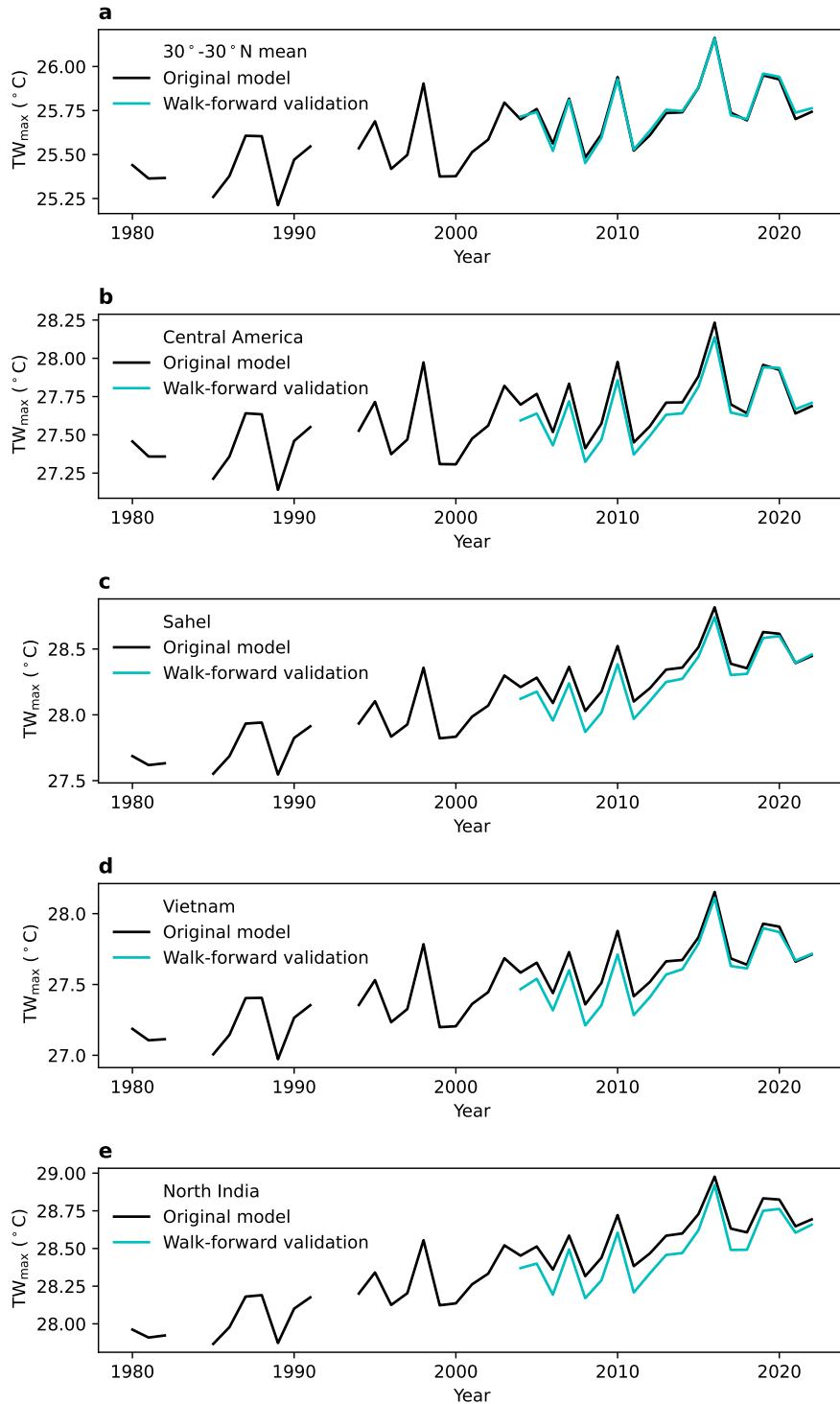


**Figure S4.** Time series of predicted  $TW_{\max}$  from the original model with all the 39 data points and that from walk-forward validation for the  $30^{\circ}\text{S}$ - $30^{\circ}\text{N}$  land average (a) and for each of the four defined regions of interest (b-e). The initial training set contains the first 20 data points. The missing points are the post-volcanic eruption years.

October 24, 2023, 9:54pm